Actuation Modeling of a Microfluidically Reconfigurable Radiofrequency Device

David Parsi[1], Jason B Metten[1], Kade Waite[1], Daniel Maynes[1], Nathan B. Crane[1]

[1]*Department of Mechanical Engineering, Brigham Young University, 350 Engineering Building, Provo, UT 84602, USA.*
bparsi@byu.edu; jbmetten@byu.edu; ckw42@byu.edu; maynes@byu.edu; nbcrane@byu.edu

Abstract

Microfluidic-based techniques have been shown to address limitations of reconfigurable radio frequency (RF) antennas and filters in efficiency, power handling capability, cost, and frequency tuning. However, the current devices suffer from significant integration challenges associated with packaging, actuation, and control. Recent advances in reconfigurable microfluidics that utilize the motion of a selectively metalized plate (SMP) for RF tuning have demonstrated promising RF capabilities but have exposed a need for an accurate fluid actuation model. This research presents a model for the mechanical motion of a moving plate in a channel to relate the SMP size, microfluidic channel size, velocity, and inlet pressure. This model facilitates understanding of the actuation response of an RF tuning system based on a moving plate independent of the actuation method. This model is validated using a millimeter-scale plate driven by a gravitational pressure head as a quasi-static pressure source. Measurements of the prototyped device show excellent agreement with the analytical model; thus, the designer can utilize the presented model for designing and optimizing a microfluidic-based reconfigurable RF device and selecting actuation methods to meet desired outcomes. To examine model accuracy at device scale, recent papers in the microfluidics reconfigurable RF area have been studied, and excellent agreement between our proposed model and the literature data is observed.

Keywords: Microfluidic channel; Microfluidic reconfigurable radio frequency; Selectively metalized plate; Micropump.

I. Introduction

The concept of microfluidics was introduced more than seventy years ago, with the advent of the inkjet printing nozzle by IBM [1]. Microfluidic devices offer fast reaction times due to their reduced diffusion distances, precise fluid control, and small reaction volumes. These devices enable rapid and efficient chemical or biochemical reactions, making them valuable for applications such as chemical synthesis, diagnostics, and drug discovery. Their ability to integrate sensors, parallelize reactions, and control temperature also contributes to their effectiveness in achieving faster reaction rates [2]. Later Gravesen et al. [3] reported on microelectromechanical pump technologies and possible actuation concepts. Afterward, many new fabrication micropump techniques have been developed that can be grouped into three primary concepts: mechanical, electro kinetic, and magneto-kinetic micropumps [4].

In mechanical micropumps, mechanical motion produces the required pressure. Mechanical micropumps can be categorized into moving diaphragm micropumps, rotary micropumps, and peristaltic micropumps [5]. Electrokinetic and magnetokinetic micropumps work based on the conversion of electrical or magnetic energy to fluid movement. They generate gradients in either electrical or conductivity permittivity of the working fluid. A recent micromachined electrohydrodynamic system was proposed by Russel et al. [6]. They surveyed different methods for enhancing system performance, such as the number of interdigitated electrode pairs, electrode surface topology, the effect of doping ferrocene in the working fluid, and the effect of external flow on the discharge characteristics.

A literature survey of recent statistics regarding wireless networks worldwide reveals that more than five billion devices demand wireless connections to run voice, data, and other applications. One active component is a RF switch, a device that routes high-frequency signals through transmission paths. An RF switch is commonly used in microwave systems for signal routing between instruments and devices. Nowadays, RF configuration can be achieved whether by microelectromechanical systems (MEMS) switches, MEMS capacitors, material loading method, varactors, PIN diodes, or ferroelectric varactors. Although these methods yield good performance in terms of speed, cost, and size, they are limited in power handling capability, radiation efficiency, and tuning range [7].

Alternatively, by integrating microelectromechanical pumping technologies with a radiofrequency device (RF), RF switches and other active devices can be actuated based on microfluidics. Microfluidics devices can be utilized to reconfigure the RF signals by pumping conductive fluids such as liquid metals [7]. Dey et al presented a microfluidically reconfigured frequency-tunable liquid-metal monopole antenna [8]. The system relied on continuous movement of the liquid metal over the capacitively coupled microstrip line. Current microfluidic-based devices have been mostly limited to frequencies well below 10 GHz due to challenges with RF modeling, utilization of liquid metals, and their inherent limitations in terms of lower conductivity and reliability [7], [9]–[11]. In addition, most recent papers focus on electronic aspects of designing microfluidically reconfigurable RF devices that are actuated by manual syringe pumps. For instance, in 2018, Kataria et al designed a reconfigurable microfluidic filter based on ring resonators [12]. Their device employed eutectic gallium indium liquid metal mixed with sodium hydroxide for improvement in the liquid metal fluidity. However, their device was actuated by ten separate manual syringe pumps [12].

Recently Mumcu and coworkers have introduced the concept of selectively metalized plates (SMP) that move within microfluidic channels to realize reliable devices with superior efficiency and power handling capabilities [[13], [14]]. Their works have used commercial micropumps (Bartels mp-6 piezo pumps) [14], [15]. Another recent study by Enrique Gonzalez-Carvajal et al. [15]presented a mm-wave tunable microfluidic reconfiguration bandpass filter. In this work the researchers used FC-40 in a microfluidic channel to move the SMP using a piezoelectric disk to pump fluid between two reservoirs. In their work, the channel and SMP sizes were not optimized.

An improved understanding of the channel, fluid, and SMP parameters can improve the reconfiguration speed of such a pump [15]. Abhishek Dey et al. designed a microfluidic broadband tunable metallic liquid monopole antenna [16], but again, the influence of the channel, liquid, and SMP parameters on the response was not explored.

A literature survey of the recent advances in the microfluidic reconfigurable RF area reveals a lack of an accurate fluid mechanics model of the actuation dynamics. Such a model would enable faster development of systems with higher performance and is the focus of this paper. In particular, this paper explores the dynamic response of an SMP in a fluidic channel and how it is influenced by SMP and fluidic channel dimensions, upstream and downstream reservior sizes, fluid viscosity, and actuation pressure. The model allows rapid estimatioun of critical design parameters so that RF designers can optimize a microfluidic-based reconfigurable RF devices. As an input the designer specifies the desired output RF-critical variables, including desired SMP size, SMP response time and SMP speed etc. The designer can then specify input variables that include microfluidic channel size, fluid properties, driving pressure actuation, etc. Then the designer can solve the analytical model presented here to calculate the response time, SMP velocities, etc. and compare these results with the desired design values.

The remainder of this paper is organized as follows. In section II, a dynamical model of SMP actuation response is presented as a function of all geometric and fluid parameters. Experiments that validate the model were also performed and Section III presents the experimental setup and approach. Section IV provides a comparison between the analytical model and experimental results. Also, comparisons with literature data from some device scale RF devices are also presented in this section. Finally, Conclusions of the work are given in section V.

II. Analytical Model

In this section an analytic model of the SMP response in a microfluidic channel will be presented. Figure 2 shows a side-view schematic of the microfluidic channel of height $2h$, width into the page of b, and length L. The SMP of length l is surrounded by the working fluid (of density ρ and viscosity μ) and is able to move horizontally between the two "channel stoppers" shown in the figure. When a positive pressure difference (denoted here as an initial equivalent height difference between the two reservoirs, H_0) is applied between the upstream and downstream reservoirs, fluid will move from the upstream to downstream reservoir, causing SMP motion as the height difference between the two reservoirs moves toward equilibrium. Leakage of fluid between the SMP and the channel walls exists, which depends strongly on the gap width δ. The fluid velocity in the channel varies across the channel width and is a maximum at the center of the channel and is zero at the top and bottom walls due to the classic no-slip fluid condition. The gap width δ affects both the amount of fluid leakage around the SMP and the shear stress that resists SMP motion, with decreasing δ resulting in higher shear stress and smaller leakage. All of the variables utilized in the model are defined in Table I.

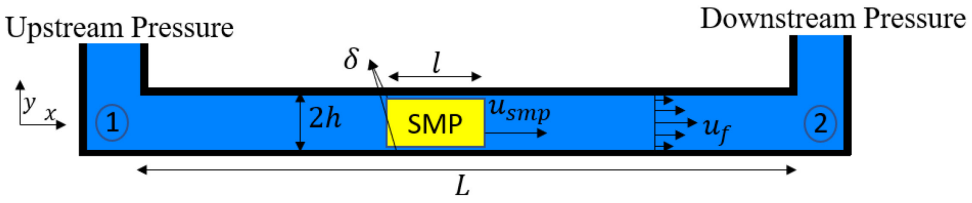

Figure 1. Side-view schematic of the fluidic channel.

Table I. Variable definitions of all parameters included in the actuation model.

μ	Fluid viscosity
ρ	Fluid density
δ	Gap width
Δp	Pressure difference between inlet and outlet
t	time
u_{gap}	Velocity of the fluid in the gap
$\bar{u}_{gap}$	Average velocity of the fluid in the gap
u_f	Velocity of the fluid in the channel
$\bar{u}_f$	Average velocity of the fluid in the channel
u_{smp}	Velocity of SMP
L	Length of channel
m_{smp}	Mass of SMP
m_f	Mass of fluid in the system
$H_0 = \frac{\Delta p}{\rho g}$	Initial equivalent height difference of the two reservoirs
D	Diameter of fluid reservoir
l	Length of SMP
h	Height of channel (Half-length)
b	Width of channel

When a pressure difference between the two reservoirs is applied, acceleration of all of the fluid in the channel and the SMP will occur. Simultaneously shear forces exerted by the channel walls on the fluid exist as the fluid moves and causes flow resistance. Shear forces exist on all walls, but the local shear stress is inversely related to the spacing between solid walls. Since the gap width δ is much smaller than the channel spacing $2h$, the fluid shear forces along the length of the SMP dominate all of the shear stresses and thus we consider only the shear that exists in the gaps between the SMP and the channel walls. To account for the shear stress that prevails on the channel walls along the length of the SMP, an expression for the transient fluid velocity distribution in the gap is needed. Thus, determining the transient fluid velocity distribution in the gap region will be considered first. Subsequently, control volume formulations of the conservation of mass and linear momentum principles will be developed.

Figure 3 shows the side view of the SMP inside the channel. It is assumed that the gap width, δ, is small compared to the length of the SMP. As a result, any minor entrance and exit effects at the leading and trailing ends of the SMP are neglected and the liquid flow in the gap between the SMP and channel walls is considered to be fully developed. Corresponding to this assumption, the wall-normal velocity is negligibly small and so are all gradients of the streamwise velocity in the x-direction. Further, the width of the SMP is much larger than the height ($b >> h$) and the z-velocity (into the page) is zero. Under the assumptions state above, and treating the fluid density and viscosity as constants, the transient partial differential momentum equation for the fluid in the gap space simplifies to:

$$\rho \frac{\partial u_{gap}}{\partial t} + \frac{dp}{dx} = \mu \frac{\partial^2 u_{gap}}{\partial y^2} \tag{1}$$

where $\frac{dp}{dx}$ is the constant homogeneous pressure gradient along the channel of length L and is equal to -$\Delta p/L$. $u_{gap}(y,t)$ is the velocity of fluid in the gap and varies as a function of time and the wall-normal coordinate y.

Equation 1 is a non-homogeneous partial differential equation subject to the no-slip boundary conditions of $u_{gap}(y=0,t)=0$, and $u_{gap}(y=\delta,t)=u_{smp}$, and the initial condition $u_{gap}(y,t=0)=0$ Equation 1 may be solved using the principle of superposition by alternately solving auxiliary homogenous problems and utilizing the classical separation of variables approach. The final solution can be written as:

$$u_{gap}(y,t) = \frac{u_{smp}y}{\delta}\left(1 + \frac{2}{\pi}\sum_{n=0}\frac{(-1)^n}{n} e^{-\frac{n^2\pi^2}{\delta^2}\left(\frac{\mu}{\rho}\right)t} \sin\left(\frac{n\pi y}{\delta}\right)\right) + \left(-\frac{\delta^2}{\mu}\left(\frac{\Delta p}{l}\right)\right)\left(\frac{1}{2}\left(1-\left(\frac{y}{\delta}\right)^2\right) - 2\sum_{n=1}\frac{\sin\frac{(2n-1)\pi}{2}}{\left(\frac{(2n-1)\pi}{2}\right)^3}\cos\left(\frac{(2n-1)\pi y}{2\delta}\right) e^{-\left(\frac{(2n-1)\pi}{\delta}\right)^2\left(\frac{\mu}{\rho}\right)t}\right) \tag{2}$$

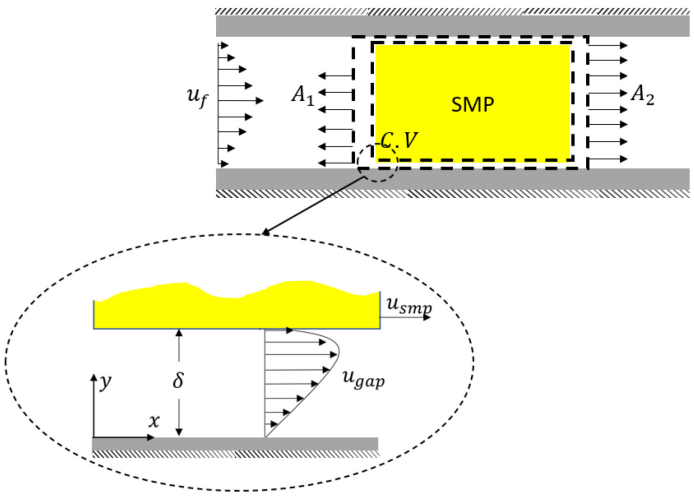

Figure 2. Side view schematic of the velocity profile for fully developed laminar flow between the SMP and channel walls.

In this model, the height of SMP is much smaller than width and the leakage along the top and bottom of the SMP is much greater than that around the sides. Thus, the side leakage is neglected. Applying ta control volume formulation of the conservation of mass principle states that the rate of mass decrease in the upstream reservoir must be balanced by the mass flow through the channel. This is expressed as:

$$\frac{\mathrm{d}H}{\mathrm{d}t}A_{res} = u_{smp}A_{smp} + Q_{gap} \tag{3}$$

where H is the height difference between the upstream and downstream reservoirs, A_{res} is the area of the reservoir, and A_{smp} is the cross-section area of SMP. Q_{gap} represents the fluid leakage around the SMP and is determined from the fluid velocity field in the gap as

$$Q_{gap} = 2b\int_0^{\delta} u_{gap}dy \tag{4}$$

A linear momentum balance using the control volume shown in Fig. 2 is now given below.

$$\gamma HA - 2\mu bl\frac{du_{gap}(y=0)}{dy} = (\acute{m}_f + \acute{m}_{f\_res}\frac{A}{A_{res}} + \acute{m}_{f\_outlet}\frac{A}{A_{out}})\frac{d\bar{u}_f}{dt} + m_{smp}\frac{du_{smp}}{dt} \tag{5}$$

The first term on the left side of the equation represents the driving pressure force due to the pressure differential that exists between the front and back of the SMP. The second term is the resisting shear force that exists on the channel walls along the length of the SMP. The terms on the right side of the equation represent the fluid and SMP masses multiplied by their respective accelerations. In equation 5, γH is the driving pressure that is imposed due to an external source like an actuator, A is the cross-section area of the channel, $\acute{m}_f$ is the total mass of fluid in the channel, $\acute{m}_{f\_res}$ is the total mass of fluid in the upstream reservoir, $\acute{m}_{f\_outlet}$ is the mass of fluid in the outlet reservoir, m_{smp} is the mass of the SMP, $\bar{u}_f$ is the average velocity of the fluid in the channel, h is the height of the channel, and b is the width of the channel.

In this study, we consider that the applied pressure is caused by a difference in heights between the up and downstream reservoirs. However, based on the required flow rate and time response, the designer can select a commercial micro pump and use its performance curve to input the pump head as the differential pressure into equation 5 . Substitution of equation 2 into equations 4 and 5 and then substituting equation 4 into equation 3 results in equations 6 and 7. These are two initial value ordinary differential equations that can be solved numerically. The initial conditions are that $H = H_0$ and $u_{smp} = 0$ at $t = 0$. Solution of the two equation yields H and u_{smp} as functions of time.

$$\frac{\mathrm{d}H}{\mathrm{d}t}A_{tank} = u_{smp}A_{smp} + bu_{smp}\delta\left(1 - \frac{8}{\pi^2}\sum_{n=0}\frac{1}{(2n+1)^2}e^{-\frac{(2n+1)^2\pi^2}{\delta^2}\left(\frac{\mu}{\rho}\right)t}\right) + 2b\delta(-(\frac{\delta^2}{4\mu}\left(\frac{\Delta p}{l}\right)(\frac{1}{3} - 2\sum_{n=1}\frac{\sin^2\frac{(2n-1)\pi}{2}}{\left(\frac{(2n-1)\pi}{2}\right)^4}e^{-\left(\frac{(2n-1)\pi}{\delta}\right)^2\left(\frac{\mu}{\rho}\right)t} \tag{6}$$

$$\gamma HA - \frac{2\mu bl}{\delta}\left(u_{smp} + 2u_{smp}\sum_{n=1}(-1)^n e^{-\frac{n^2\pi^2}{\delta^2}\left(\frac{\mu}{\rho}\right)t} - \frac{\delta^2}{4\mu}\frac{\Delta p}{l}\left(-1 + 2\sum_{n=1}\frac{\sin\frac{(2n-1)\pi}{2}}{\frac{((2n-1)\pi)^2}{8}}\sin\left(\frac{(2n-1)\pi}{2}\right)e^{-\left(\frac{(2n-1)\pi}{\delta}\right)^2\left(\frac{\mu}{\rho}\right)t}\right)\right) = m_f\frac{d\bar{u}_f}{dt} + m_{smp}\frac{du_{smp}}{dt} \quad (7)$$

In order to reduce the total number of independent variables contained in equations 6 and 7, classical nondimensionalization is performed and equations 8 and 9 represent non-dimensional versions of equations 6 and 7. The dimensionless forms of all variables are shown in Table II.

Table II. Dimensionless parameters for the actuation model of equations 8 and 9.

Variable type	Description	Dimensionless Variable	Definition
Dependent variables	Dimensionless SMP velocity	U^*_{smp}	$\frac{\mu u_{smp}}{\rho g\delta^2}$
	Dimensionless fluid velocity	U^*_f	$\frac{\mu \bar{u}_f}{\rho g\delta^2}$
	Dimensionless reservoir height	H^*	$\frac{H}{H_0}$
Independent variables	Dimensionless time	τ	$\frac{\mu t}{\rho\delta^2}$
	Dimensionless SMP mass	M^*_{smp}	$\frac{m_{smp}}{2hb\rho H_o}$
	Dimensionless fluid mass	M^*_f	$\frac{m_f}{2hb\rho H_o}$
	Dimensionless SMP length	L^*	$\frac{l}{H_0}$
	Dimensionless channel gap	δ^*	$\frac{\delta}{2h}$
	A generalized dimensionless variable	π_0	$\frac{\rho^2 gb\delta^5}{\mu^2 lA_{res}}$

$$\frac{dH^*}{d\tau} = 2\pi_0 L^* U^*_{smp}(1-2\delta^*)/\delta^* + \pi_0 L^* U^*_{smp}\left(1 - \frac{8}{\pi^2}\sum_{n=0}\frac{1}{(2n+1)^2}e^{-(2n+1)^2\pi^2\tau}\right) - \frac{\pi_0}{2}H^*\left(\frac{1}{3} - 2\sum_{n=1}\frac{\sin^2\frac{(2n-1)\pi}{2}}{\left(\frac{(2n-1)\pi}{2}\right)^4}e^{-\left(\frac{(2n-1)\pi}{1}\right)^2\tau}\right) \quad (8)$$

$$H^* - \left(2L^*\delta^* U^*_{smp}\left(1 + 2\sum_{n=1}(-1)^n e^{-\frac{n^2\pi^2}{1}\tau}\right) - H^*\delta^*\left(-1 + 2\sum_{n=1}\frac{\sin\frac{(2n-1)\pi}{2}}{\frac{((2n-1)\pi)^2}{8}}\sin\left(\frac{(2n-1)\pi}{2}\right)e^{-\left(\frac{(2n-1)\pi}{1}\right)^2\tau}\right)\right) = M^*_f\frac{dU^*_f}{d\tau} + M^*_{smp}\frac{dU^*_{smp}}{d\tau} \quad (9)$$

The analytical model described above was exercised over the range of physical parameters that are shown in Table III and some representative results of this process will be presented and

discussed in this section. Figure 3a shows the dimensionless SMP velocity, U^*_{smp} as a function of the dimensionless time, $\underline{\tau}$. For the results shown in Figure 3a, the dimensionless SMP mass, SMP length, and dimensionless fluid mass were held constant at the values shown in Table IV and the dimensionless gap size, δ^*, was allowed to vary from 0.015 to 0.12. This variation corresponds to a physical gap that varied between 3% and 24% of the channel height. The results of Figure 3a reveal that all of the U^*_{smp} data lie on a single curve and thus for these conditions the U^*_{smp} vs. τ curve is not dependent on the value of δ^*. Further, the data show that the steady state (maximum) SMP velocity is attained at a non-dimensional time of $\tau \approx 1.4$ and that the steady state value of U^* is approximately 0.206.

The influence of varying the dimensionless SMP mass and the dimensionless SMP are illustrated in Figures 3b and 3c. Shown in Figure 3b is the dimensionless SMP velocity as a function of τ for several values of M^*_{smp} and at constant values of M^*_f, L^*, and δ^*, as shown in Table IV. Here the data show, as expected, the steady state value of U^*_{smp} increases as the mass of the SMP decreases, due to the smaller inertia of the SMP relative to the driving pressure force. For example, a 50% decrease in M^*_{smp} results in a 124% increase in the steady state value of U^*_{smp}. Shown in Figure 3c is U^*_{smp} as a function of τ over a range of L^* values, with the other independent parameters fixed as specified in Table IV. As L^* increases the steady state speed of the SMP decreases. This is caused by the increased shear force that prevails due to increased SMP surface area.

Interestingly, while the data of Figures 3b and 3c show that the steady state value of U^*_{smp} depends strongly on $L^*$and M^*_{smp}, the value of τ required for the steady state speed to be reached is independent of both of these values. In fact, the value of τ when the SMP velocity is within 5% of its steady state value is τ = 1.45 and this value is independent of the value of any of the other independent dimensionless variables listed in Table IV. The importance of this is that the dimensional time required for the SMP to attain its maximum velocity is easily predicted as $t = 1.45\rho\delta^2/\mu$. Thus, as the gap between the SMP and channel walls decreases, the response time decreases as well and increasing the viscosity of the liquid in the fluidic channel will yield an increase in the response time. It should be noted that for the results presented here the smallest gap width considered was 3% of the channel height and this value was chosen based on the limitations prevalent in the manufacture of real devices.

Table III. The dimensions and material that used in the model.

Fluid type	$D(m)$	$h(m)$	$\mu\ (Pa.s)$	$\delta\ (m)$	$b(m)$	$H_0(m)$
Mixture of water and glycerol	0.074	$0.001 - 0.008$	$0.001 - 0.008$	$0.00024 - 0.0012$	$0.005 - 0.03$	$0.17133 - 0.70$

Table IV. Fixed and varying dimensionless parameters corresponding to Figure 3 and Figure 4

Figure number	$\mathbf{M^*_{smp}}$	$\mathbf{M^*_f}$	$\mathbf{L^*}$	$\boldsymbol{\delta^*}$	π_0
Figure 3a	0.1815	74.43	0.1765	0.12-0.015	$0.000874\text{-}2.6 \times 10^{-8}$

Figure 3b	0.047-0.194	74.43	0.1765	0.12	0.000874
Figure 3c	0.1815	74.43	0.063-0.428	0.12	0.000874
Figure 4a	0.047-1.48	74.43-110	0.1765	0.12	0.000874
Figure 4b	0.1815	74.43	0-1	0.12-0.015	$0.000874\text{-}2.6 \times 10^{-8}$

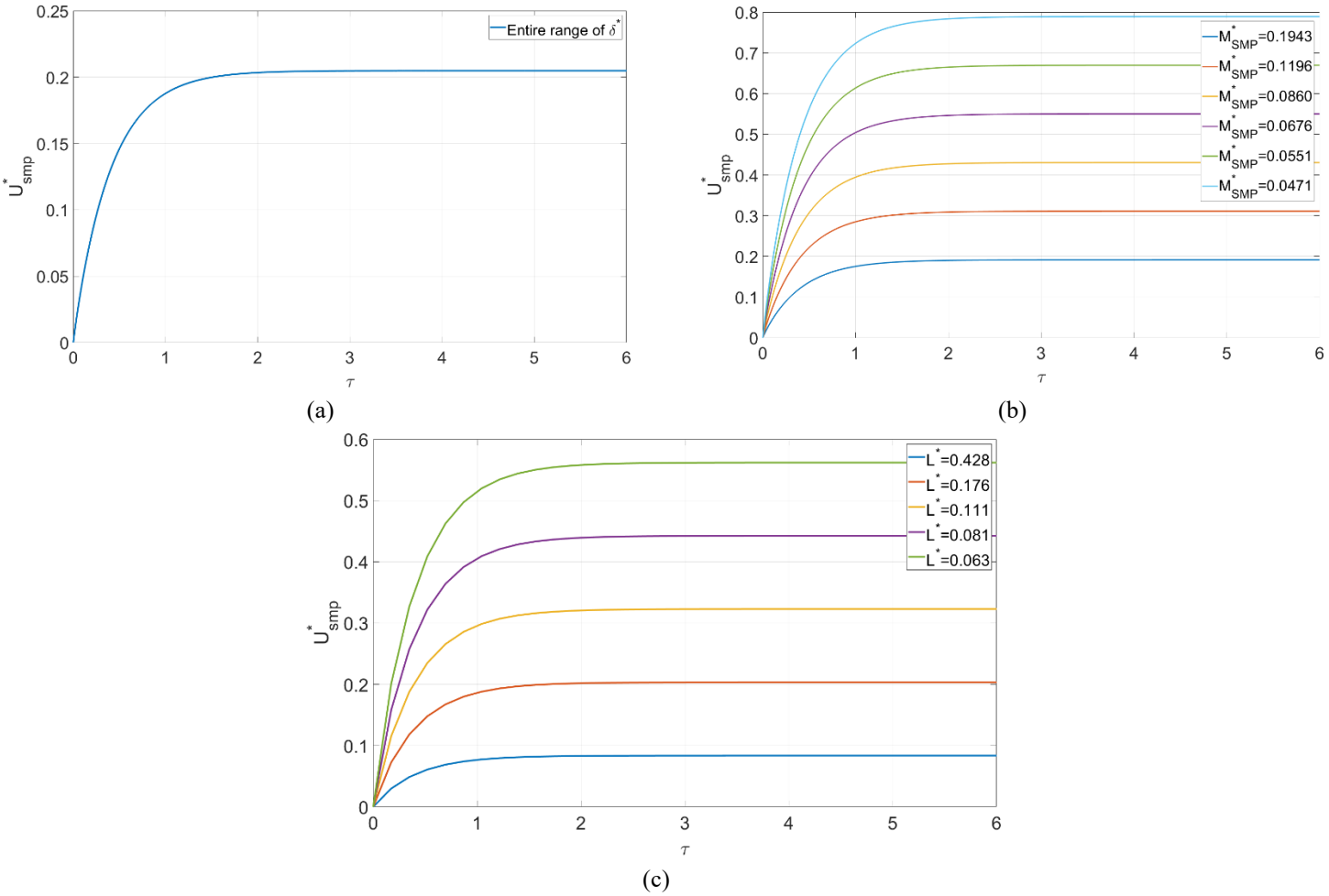

Figure 3. Dimensionless SMP velocity as a function of τ for varying a) dimensionless channel gap, b) dimensionless SMP mass, and c) dimensionless channel length. The other independent dimensionless parameters were held constant as shown in Table IV.

The analytical model was exercised over the entire range of parameters shown in Table III and the resulting independent dimensionless variables. The purpose of this was to understand how the steady state (maximum) SMP velocity varies as a function of all variables. An example of these simulations is shown in Figures 4a and 4b. Figure 4a shows the steady-state value of the dimensionless SMP velocity, $U^*_{smp\text{-}ss}$ as a function of the dimensionless SMP mass, $M^*_{smp.}$ for values of M^*_f varying as shown in the figure legend. The results shows that $U^*_{smp\text{-}ss}$ increases following an inverse power law relation as M^*_{smp} decreases. Decreasing M^*_{smp} can be accomplished by decreasing the SMP mass, increasing the driving height difference between the two reservoirs (driving pressure), and increasing the height or width of the fluidic channel. Figure 4b shows

$U^*_{smp\text{-}ss}$ as a function of the dimensionless SMP length and the results clearly show that the steady-state velocity of SMP increases as L^* decreased, which can be accomplished either by decreasing the SMP length or increasing the driving pressure.

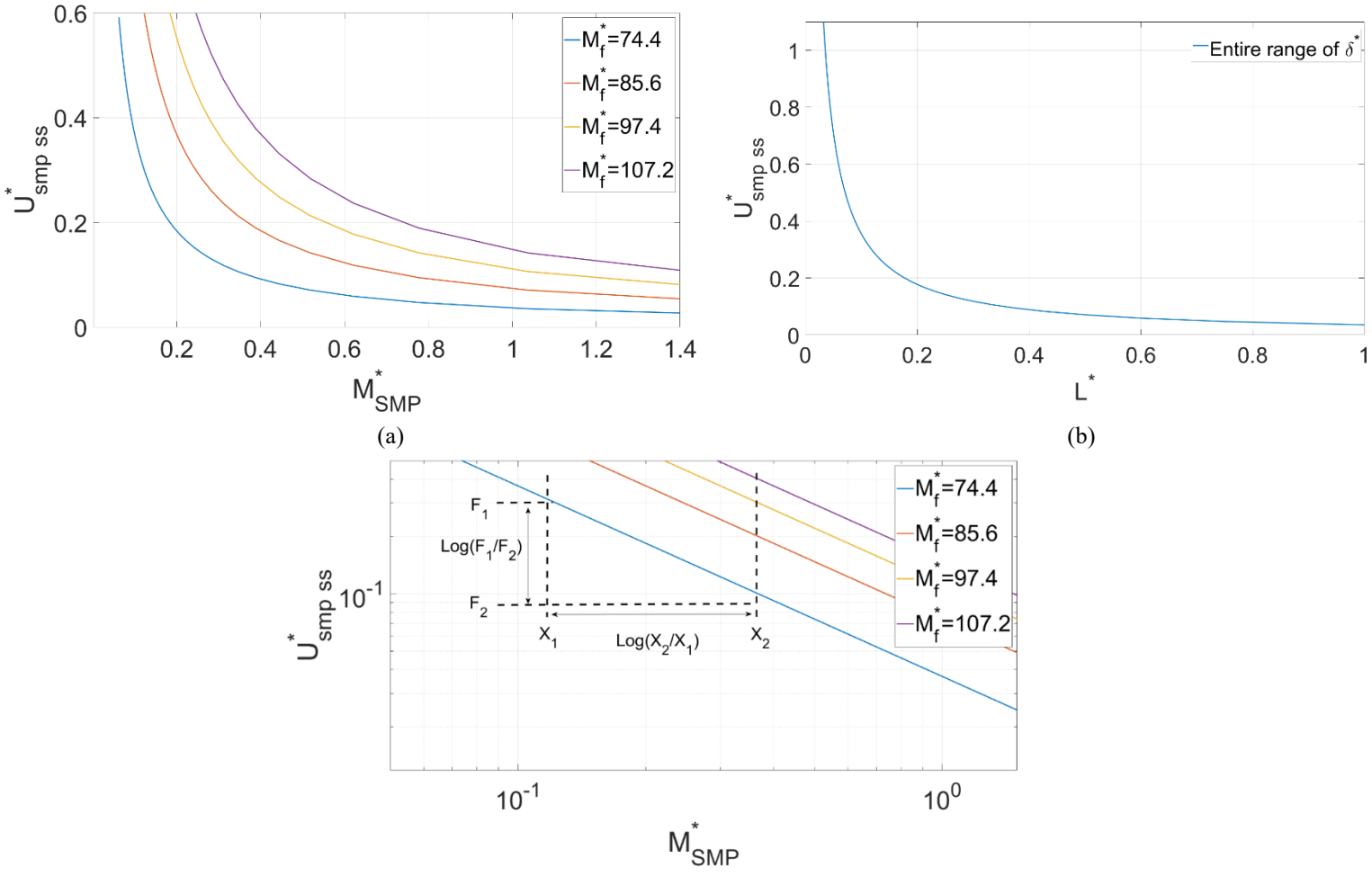

Figure 4. $U^*_{smp\text{-}ss}$ as a function of a) dimensionless SMP mass (M^*_{smp}) b) dimensionless SMP length (L^*) c) $U^*_{smp\text{-}ss}$ as a function of M^*_{smp} on a log–log scale.

To further study the behaviour the steady-state velocity of the SMP a log-log plot is useful. Figure 4c shows the log-log normalized SMP steady-state velocity as a function of the dimensionless SMP mass (M^*_{smp}). Here, the dependence between $U^*_{smp\text{-}ss}$ and M^*_{smp} are straight lines on the log-log plot, implying a power-law relationship between them as follows:

$$U^*_{SMP-ss} = C_1\left(M^*_{smp}\right)^{C_2} \tag{10}$$

where C_1 and C_2 are constant coefficients that can be calculated from results from the model.

The significance of Equation 10 lies in its ability to quickly estimate U^*_{SMP-ss} for any given scenario, obviating the need for solving the comprehensive analytical model outlined earlier (Equations (8-9)). In this manner, a general steady-state velocity of the system can be expressed

as a combination of power law relations. A multidimensional linear regression analysis was performed to determine a power law relation that captures the influence all of the independent non-dimensional parameters on the value of $U^*_{smp\text{-}ss}$ and this is shown below as Equation 11. Note that the variables $\delta^*$and π_0 exercise negligible influence on $U^*_{smp\text{-}ss}$. To assess the precision of the regression model for swiftly estimating steady-state velocity, we compared the dimensionless steady-state velocity, computed using Equation 11, with values derived from the analytical model (Equations 8-9), as shown in Figure 5. The root mean square error between Equation 11 and Equations 8-9 was found to be 3.95%. The importance of Equation 11 is that it allows rapid estimation of $U^*_{smp\text{-}ss}$ for any scenario without ever having to solve the complete analytical model described above. It was observed above that for all scenarios the nondimensional time when steady state is attained is $\tau = 1.45$ and combined with Equation 1 the designer can easily determine the temporal response and steady state speed of an SMP actuated by a pressure source as functions of all of the geometric and fluid variables.

$$U^*_{SMP-ss} = 2.81 \times 10^{-12}\left(M^*_{smp}\right)^{-1}\left(\mathrm{M}^*_f\right)^5(\mathrm{L}^*)^{-1} \tag{11}$$

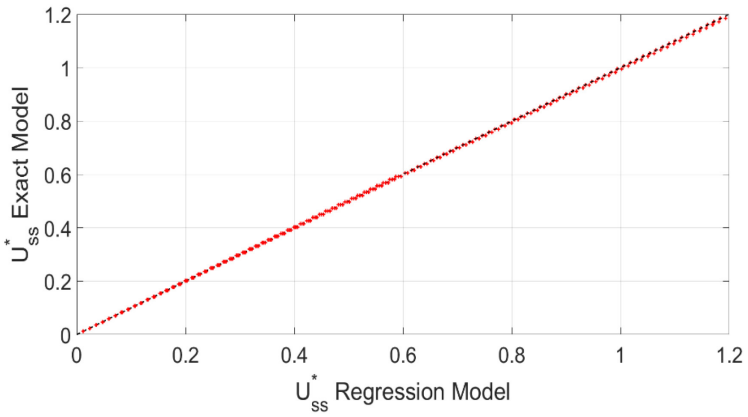

Figure 5 comparison between $U^*_{smp\text{-}ss}$ values obtained from the exact solution and regression model.

In practice the designer can follow the process illustrated in the process diagram shown in Figure 6 to select geometric sizes for the specific application. The process begins with specifiying the initial values for the geometric and fluid variables such as channel size, gap size, working fluid, driving pressure, etc. The designer can then select a commercial micro pump and use its performance curve to calculate the differential pressure that the selected pump can provide. For instance, Fang et al reported a performance curve for a micro pump for both water and oil as a working fluid [17]. After selecting the input pressure source, the designer can calculate the dimensionless parameters shown in Table II, and check the actual time constant. Then the steady state speed of the SMP response can be calculated by Equation 11. The time constant and steady state speed can then be compared to the design requirments and then the process can be repeated to yield SMP speed and time response that fits the specific desgin. In this manner the design knowledge accumulated from the analytical model and regression results are highly valuable in

the practical design process so that the designer can quickly identify variable values for a SMP design and actuation to reach a required SMP velocity.

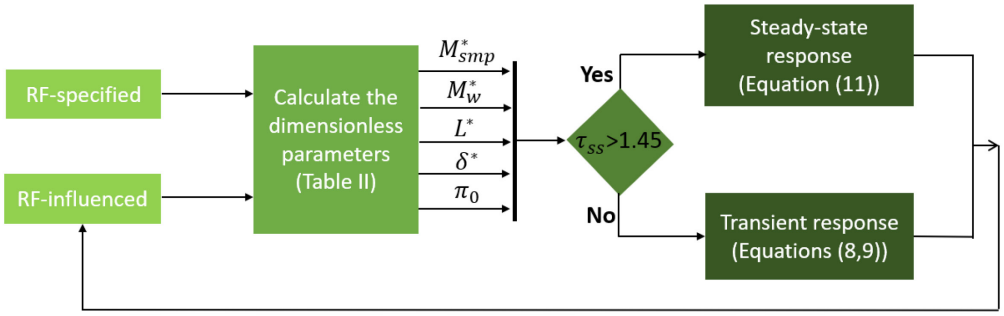

Figure 6. The flowchart of the design process.

III. Experimental setup and Results

In microscale fabrication, subtractive techniques such as etching, and photolithography can be utilized to fabricate microfluidic channels in silicon or glass [18]. Recently, a wide range of interest has been focused additive manufacturing (AM) (i.e., 3D printing techniques). In this study, we have deployed AM techniques in addition to traditional CNC machining to make a millimetre scale model of the microfluidic channel and SMP. Figure 7 shows the schematic figure of the proposed channel designed in addition to the actuation method and measuring techniques. The SMP can move in the channel which is connected to a pressure source by a valve. In order to decrease the model parameter uncertainty, a simple actuation method is selected with a nearly constant gravitational pressure from a large diameter reservior. A high-speed camera is utilized to the measure the velocity of the SMP and the volumetric flow rate.

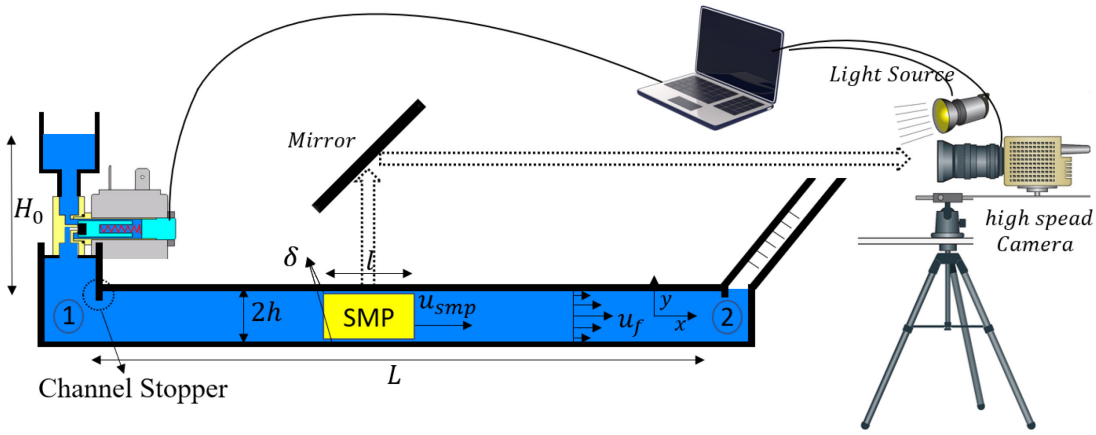

Figure 7. The schematic model of the proposed experimental model.

Figure 8 shows the prototype. In this study, the experimental data has explored the effects of varying flow viscosity, and potential force in addition to the effects of channel height, gap size, SMP size, and SMP mass.

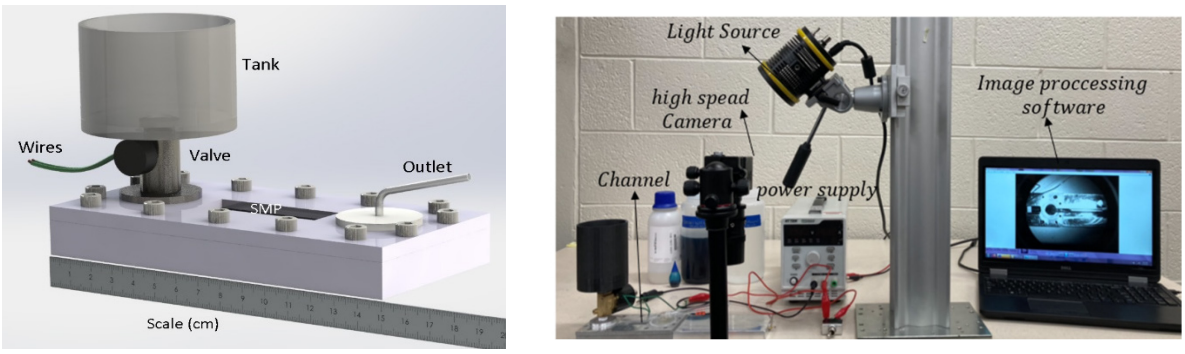

Figure 8. The isometric view of the proposed model and experimental setup.

The SMP is fabricated by SLA resin with an embedded magnet to help to reset the position of SMP after each test and increase the plate density. Figure 9 shows the SMP position inside of channel both in the rest position and under acceleration. As illustrated in Figure 9, the SMP moving through the channel is subject to a locking mechanism based on friction called "wedging and jamming" [19]. Asymmetry in the drag and/or acceleration forces will rotate the SMP until it contacts the edges and lock the system due to friction. In order to overcome these drawbacks four small feet were added to the SMP to align the plate to the channel with minimal friction.

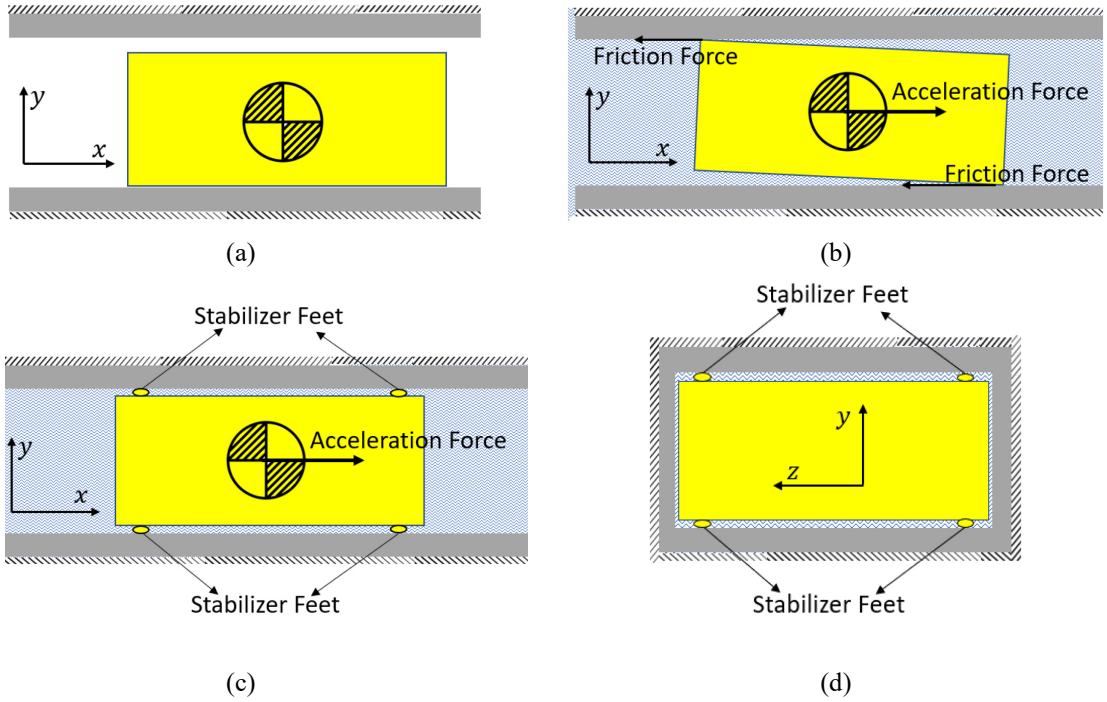

Figure 9. The side-view of SMP in the channel a) at asymmetry rest position, b) under acceleration, the schematic view of SMP in the channel under acceleration with stabilizer feet, c) side-view, d) front-view.

The case-study tactics and design knowledge accumulated from the analytical model are highly valuable if they can verify the experimental data. In order to verify the analytical model,

the system of ordinary differential equation initial value problems (Equations 8, and 9) is solved numerically using the parameters from Tables II.

The test begins by filling the large cylindrical reservoir with fluid to a specific the height required to obtain a desired actuation pressure. The moving plate is positioned in its starting position. To start the test, a trigger synchronizes the start of the camera footage and opens the valve. The high-speed camera measures both position of the fluid in the outlet pipe and the position of the SMP over time. Table V shows the experimental parameters.

Table V. The experimental conditions

$D(m)$	$h(m)$	$\mu\ (Pa.s)$	$\delta_{bottom}(m)$	$\delta_{top}(m)$	l(m)	$b(m)$	$H_0(m)$
0.074	0.002	0.001	0.00024	0.00024	0.01,0.02,0.025	0.03	0.17133
SMP length			20mm			25mm	
SMP weight			1.54g, 1.79g, 2.09g			1.89g, 2.17g, 2.47g	
Pressure Head			1678 pa, and 839 pa				
Working Fluid			Water ($\mu = 0.001Ns/m^2, \rho = 998kg/m^3$), 20.2% glycerol ($\mu = 0.002Ns/m^2, \rho = 1057kg/m^3$), and 36.3% glycerol ($\mu = 0.004Ns/m^2, \rho = 1100kg/m^3$)				

An experiment was conducted to study the effect of the potential driving force on SMP velocity. As can be seen in Figure 10, the experimental measurements closely match the theoretical models. Figure 10a shows the SMP velocity for different pressure heads. Decreasing the driving force by 50% only decreased the steady state velocity 34% due to the nonlinearity of this system. In the next set of experiments, the effect of fluid viscosity on SMP velocity was explored. Figure 10b shows the SMP velocity for 20.2% glycerol and 36.3% glycerol as well as water. As can be seen in this figure, the SMP steady-state velocity increases when the viscosity increases since less fluid passes through the gap between the SMP and channel wall; however, that only happened because of current combination of gap size ($h/\delta \approx 8.3$). The simulations show that with smaller gap ($h/\delta > 10.7$) the steady-state velocity will always decrease when viscosity increases. In this figure, we illustrate the influence of viscosity on fluid behavior. During the tests conducted with a 36.3% glycerol solution, noticeable errors were observed due to valve opening time delays caused by the high viscosity of the fluid in the tank. However, once the valve is fully open, the system reaches a steady-state stage, and this delay does not affect the steady-state results. Additionally, we have observed the presence of more gas bubbles in the viscous fluid, which initially compresses the gas bubbles before reaching a steady-state, leading to a delay in the transient regime. Notably, in the context of RF fluidic reconfigurable devices, high-viscosity fluids are typically not utilized.

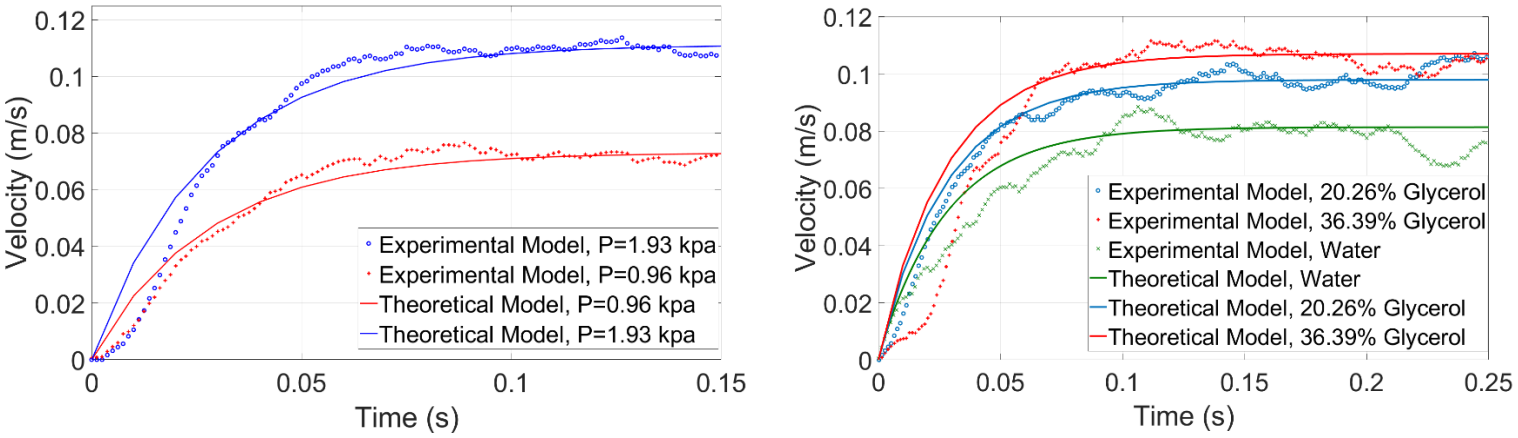

(a) (b)

Figure 10. The SMP velocity for a) different pressure heads (with 36.3% glycerol), b) different viscosities (with full pressure head).

Figure 11 shows the comparison between the experimental and theoretical approaches of SMP velocity as a function of time for various SMP masses and lengths. For instance, decreasing the length of SMP by 20% increases the steady-state velocity by 17.2% and decreasing the mass of SMP by 54% increases the steady state SMP velocity by 69.9%. Table VI shows the experimental parameters used for these tests. In addition, Figure 12 compares non-dimensional experimental and analytical models based on Tables VI. The experimental results demonstrate that the prototype can achieve excellent performance in steady-state velocity and time response; however, in the transient region, the value predicted by the experiment may be a little different from the theoretical model due to some minor losses such as reservoir valve opening time, and surface roughness which are unavoidable for large scale experiment test.

Table VI. The experimental conditions

Pressure head		**SMP Length**	**SMP weight**	**Channel height**		**Working Fluid**
1678.9 Pa		20mm, and 25mm	1.79g, 2.48g and 3.70g	4mm		Water
$\boldsymbol{D(m)}$	$\boldsymbol{h(m)}$	$\boldsymbol{\mu\ (Pa.s)}$	$\boldsymbol{\delta_{bottom}(m)}$	$\boldsymbol{\delta_{top}(m)}$	$\boldsymbol{b(m)}$	$\boldsymbol{H_0(m)}$
$\mathbf{0.074}$	0.002	0.001	0.00024	0.00024	0.03	0.17133

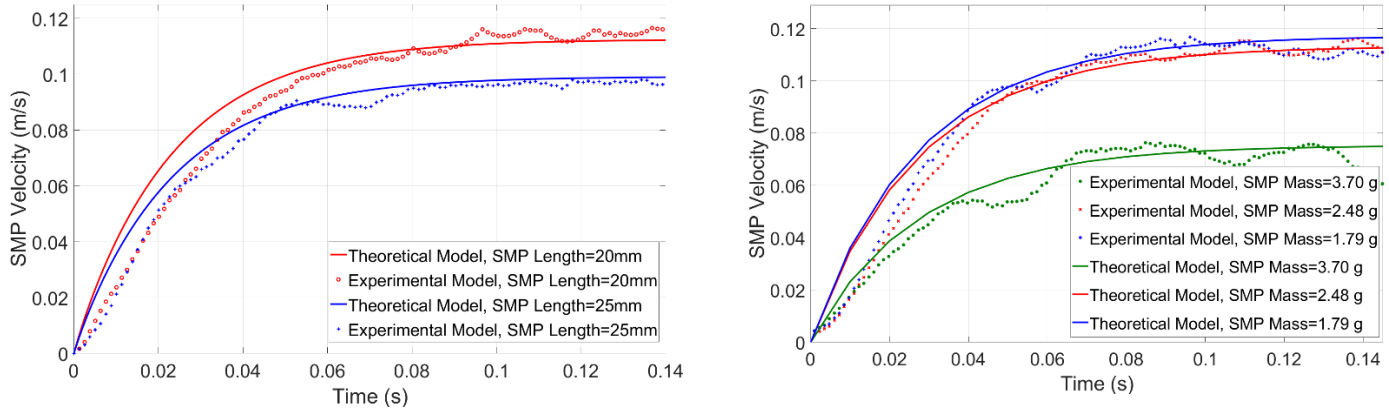

(a) (b)

Figure 11. The SMP velocity as a function of time for the different a) SMP length (SMP Mass=1.79 g), b) SMP Mass (SMP length=25mm).

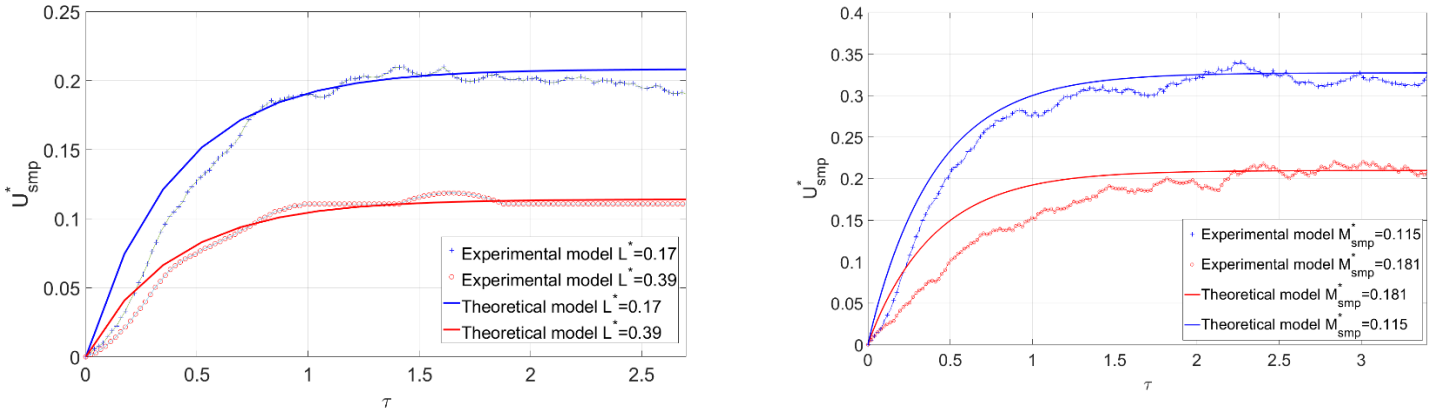

(a) (b)

Figure 12. The non-dimensional SMP velocity as a function of non-dimensional time based on Table V experimental conditions for different a) dimensionless channel lengths, b) dimensionless SMP masses.

To examine the model accuracy at the device scale, the results reported in recent papers by Mumcu and his group on SMP controlled reconfigurable microfluidics have been studied. In fact, many studies in the area of microfluidically reconfigurable RF device, do not report important actuation parameters such as flow rate and pressure, and mainly, they study the frequency and response time rather than modelling the fluid system. However, T. Palomo et al. [14] reported all required variables for the proposed model.

In this work, Bartels mp-6 piezo pumps were utilized to move SMP 11.57 mm in ~1 s, the flow rate, and pressure are 8000 $\mu l/min$, 500 $mbar$ accordingly. Their channel was made from SU8 with 275 μm thickness, and SMP thickness is 250 μm. Table VIII shows the schematic figure of their setup and reported parameters while the comparison between the proposed model and the reference model is shown in Table VII.

Table VII. Parameters that reported by references [13],[19].

References	Reported parameters

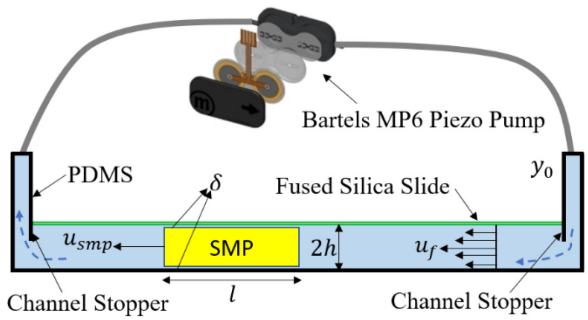

Response time 1.12ms, $l = 633\mu m, 2h = 275\mu m$ $b = 16.5mm$, and the working fluid is FC-40

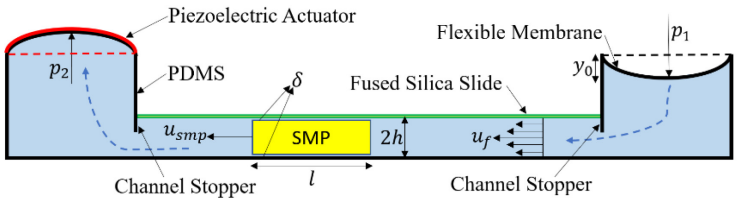

$L = 1.55mm$ $h = 275\mu m$, $b = 1.9mm$, and the working fluid is FC-40

Another highly valuable piece of work was done by González. E in 2019 [20]. In this study, the SMP located inside the microfluidic channel is repositioned with the fluid flow and actuated by a piezoelectric actuation method, Figure 13 shows the schematic model of the actuation method. However, the authors did not measure and report the working pressure. In this case, the FEM methodology can offer a highly precise result, so the COMSOL Multiphysics software will be utilized to estimate the operating pressure range for the T216-A4NO-05-piezoelectric bending disc. Figure 14 shows the pressure as a function of voltage for different membrane thickness. In the reference, the author reported the reconfiguration time 1.12 ms while 52V applied. As can be seen in this figure the estimated pressure should be between 23cpa to 142cpa for membrane thickness 100-250μm. The comparison between the proposed model and the reference model is shown in Table VIII.

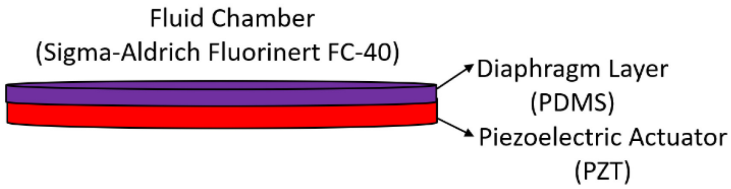

Figure 13. The schematic model of the actuation method that is used in reference [20].

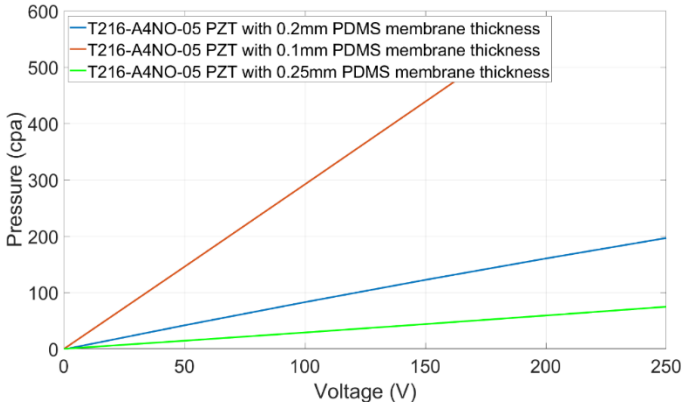

Figure 14. The pressure as a function of excitation voltage for different membrane thicknesses.

Table VIII. Comparison between our proposed model and references.

Reported and estimated parameters by references	Our Proposed Model
SMP velocity (Reference [14]) *Response time 1* $\boldsymbol{s}$*, Pressure= 500* $\boldsymbol{mbar}$*,* $\boldsymbol{h = 275\mu m}$*,* $\boldsymbol{b = 16.5mm}$*,* $\boldsymbol{\delta}$**~25** $\boldsymbol{\mu m}$*, and the working fluid is FC-40 (*$\boldsymbol{\mu = 0.004\ N.s/m^2}$)	*Response time 0.98s*
SMP velocity (Reference [20]) *Response time 1.12ms, Pressure= 23 cpa to 142 cpa,* $\boldsymbol{l = 633\mu m}$*,* $\boldsymbol{b = 1.9mm}$*,* $\boldsymbol{\delta}$**~6** $\boldsymbol{\mu m}$*, and the working fluid is FC-40 (*$\boldsymbol{\mu = 0.004\ N.s/m^2}$).	$Response\ time\ 3.76ms - 1.04ms$ $(membrane\ thickness\ 100 - 250\mu m)$

Since we were able to validate our proposed model successfully, now the proposed model can be utilized to improve the performance of the RF devices that are designed in the literature. In other words, the design knowledge accumulated from the analytical model and dimensionless parameters are highly valuable in the practical design process so that the designer can work out a specific SMP design to reach a required SMP velocity. For instance, González. E in 2019 [20] reported the response time as 1.12ms. To increase the speed of response by 50% to 0.56ms, the mass of SMP should be decreased by 42.1%, or the length of SMP should decrease by 55.6%. Moreover, our study shows that by increasing the diameter of reservoir by 20.3% the speed of response can be increased by 50% to 0.56ms or instead of increasing the diameter of reservoir which may not be feasible due to the space limitation, the designer can increase the pressure by 37.5% to reach to that result. This can be done by increasing the working voltage or changing the micropump type. Since the ratio of channel height to the gap size is greater than 10.7 ($h/\delta \approx 41$), increasing the viscosity of the working fluid decreases the actuation speed. For instance, by decreasing the viscosity by 50%, the actuation speed can be increased by 19%, so we propose to use Novec-649, instead of FC-40 to increase the actuation speed or instead of changing the working fluid, the same result can be achieved by increasing the working temperature.

IV. Conclusion and Future Works

In this paper, a design methodology for a microfluidically reconfigurable RF plate was presented. A simple actuation method was utilized in this research; however, based on the required flow rate and time response, the designer can select a commercial micro pump and use its

performance curve to calculate the head as the differential pressure that the selected pump has to overcome in order to move the fluid. To explore the parameters effect in the proposed model, the non-dimensional parameters were defined. The experimental results demonstrated that the model matched the measured performance very well in the steady-state region. By decreasing the mass of SMP by 42.1%, the steady-state velocity increases by 50%. On the other hand, when the length of SMP increases by 55.6%, the steady-state velocity decreases by 50%. Moreover, when the pressure increases 100%, the steady-state velocity increases 129%.

In addition, the linear regression analysis can quantify the strength of the relationship between the normalized steady-state velocity of SMP response and the non-dimensional parameters. The case study tactics and design knowledge accumulated from the analytical model and dimensionless parameters are highly valuable in the practical design process so that the designer can work out a specific SMP design to reach a required SMP velocity. In other words, this model facilitates understanding of the actuation response of a given RF tuning system independent of the actuator. In addition, the proposed model was verified against published work on RF devices that utilize SMP actuation with good agreement.

In future work, this analytical model can prove to be a valuable tool if applied to the conversion of a single-input/single-output transfer function within a controller unit to enable rapid prediction of frequency response characteristics. Specifically, it can be employed with pressure as the input and the velocity of SMP as the output. Integration and calibration of this model with an RF device offer the potential for users to tune the RF device without requiring in-depth knowledge of the underlying design details.

Furthermore, it's worth noting that in the current study, the development of a general analytical model was achieved. However, it was observed that errors emerged in the transient regime when comparing the model's predictions to experimental results. These discrepancies were attributed to the presence of numerous mechanical components such as valves connection elbows. To enhance the accuracy of the model in the transient regime and bridge the gap between theory and experiment, future work may involve the miniaturization of the system to a micro-scale.

sently, microfluidic-based devices predominantly rely on mechanical micropumps, including diaphragm micropumps, rotary micropumps, and peristaltic micropumps. These pumps necessitate expensive clean-room fabrication methods and are constrained in terms of their size. In light of these limitations, exploring alternative solutions such as the utilization of an Electrowetting on Dielectric (EWOD) pump holds promise. Future work could integrate models of these and other actuators to create a complete system model. Such an approach has the potential to address some of the aforementioned issues by enhancing performance and reducing costs in microfluidic systems.

Acknowledgments

The authors wish to thank Dr. Gokhan Mumcu for providing additional information on the experimental setup at the department of Electrical Engineering at the University of South Florida. The work is supported in part by the National Science Foundation thorough Grant No.1920953.

REFERENCE

[1] Yu Song, Daojian Cheng, and Liang Zhao, *Microfluidics: Fundamentals, Devices, and Applications*, 1st ed. John Wiley & Sons, Inc., 2018.

[2] F. Mi *et al.*, "Recent advancements in microfluidic chip biosensor detection of foodborne pathogenic bacteria: a review," *Analytical and Bioanalytical Chemistry*, vol. 414, no. 9. Springer Science and Business Media Deutschland GmbH, pp. 2883–2902, Apr. 01, 2022. doi: 10.1007/s00216-021-03872-w.

[3] B. Puneeth, M. B. Kulkarni, S. Goel, P. Gravesen, J. Branebjerg, and O. S. Jensen, "Microfluidics-a review You may also like Microfluidic viscometers for biochemical and biomedical applications: A review S 1 Microfluidics-a review," 1993.

[4] Y. N. Wang and L. M. Fu, "Micropumps and biomedical applications – A review," *Microelectronic Engineering*, vol. 195. Elsevier B.V., pp. 121–138, Aug. 05, 2018. doi: 10.1016/j.mee.2018.04.008.

[5] M. K. D. Manshadi, M. Mohammadi, M. Zarei, M. Saadat, and A. Sanati-Nezhad, "Induced-charge electrokinetics in microfluidics: A review on recent advancements," *Journal of Micromechanics and Microengineering*, vol. 30, no. 11. IOP Publishing Ltd, Nov. 01, 2020. doi: 10.1088/1361-6439/abaf34.

[6] M. K. Russel, P. R. Selvaganapathy, and C. Y. Ching, "Electrical discharge characteristics of a dielectric liquid under external flow in a microchannel with planar electrode configuration," *J Electrostat*, vol. 87, pp. 212–216, Jun. 2017, doi: 10.1016/j.elstat.2017.05.002.

[7] Kurmendra and R. Kumar, "A review on RF micro-electro-mechanical-systems (MEMS) switch for radio frequency applications," *Microsystem Technologies*, vol. 27, no. 7. Springer Science and Business Media Deutschland GmbH, pp. 2525–2542, Jul. 01, 2021. doi: 10.1007/s00542-020-05025-y.

[8] A. Dey, R. Guldiken, and G. Mumcu, "Microfluidically Reconfigured Wideband Frequency-Tunable Liquid-Metal Monopole Antenna," *IEEE Trans Antennas Propag*, vol. 64, no. 6, pp. 2572–2576, Jun. 2016, doi: 10.1109/TAP.2016.2551358.

[9] M. Kelley *et al.*, "Frequency reconfigurable patch antenna using liquid metal as switching mechanism," *Electron Lett*, vol. 49, no. 22, pp. 1370–1371, Oct. 2013, doi: 10.1049/el.2013.2930.

[10] A. Dey, R. Guldiken, and G. Mumcu, "Wideband frequency tunable liquid metal monopole antenna," in *IEEE Antennas and Propagation Society, AP-S International Symposium (Digest)*, 2013, pp. 392–393. doi: 10.1109/APS.2013.6710857.

[11] A. Pourghorban Saghati, J. Singh Batra, J. Kameoka, and K. Entesari, "Miniature and reconfigurable CPW folded slot antennas employing liquid-metal capacitive loading," *IEEE Trans Antennas Propag*, vol. 63, no. 9, pp. 3798–3807, Sep. 2015, doi: 10.1109/TAP.2015.2447002.

[12] T. Kaur, L. Osorio, J. L. Olvera-Cervantes, R. Reyes-Ayona, and A. Corona-Chavez, "Microfluidic reconfigurable filter based on ring resonators," *Progress in Electromagnetics Research Letters*, vol. 79, pp. 59–63, 2018, doi: 10.2528/pierl18080402.

[13] A. Qaroot and G. Mumcu, "Microfluidically Reconfigurable Reflection Phase Shifter," *IEEE Microwave and Wireless Components Letters*, vol. 28, no. 8, pp. 684–686, Aug. 2018, doi: 10.1109/LMWC.2018.2847046.

[14] T. Palomo and G. Mumcu, "Microfluidically Reconfigurable Microstrip Line Combline Filters with Wide Frequency Tuning Capabilities," *IEEE Trans Microw Theory Tech*, vol. 65, no. 10, pp. 3561–3568, Oct. 2017, doi: 10.1109/TMTT.2017.2730181.

[15] E. Gonzalez-Carvajal and G. Mumcu, "Frequency and Bandwidth Tunable mm-Wave Hairpin Bandpass Filters Using Microfluidic Reconfiguration with Integrated Actuation," *IEEE Trans Microw Theory Tech*, vol. 68, no. 9, pp. 3756–3768, Sep. 2020, doi: 10.1109/TMTT.2020.3006869.

[16] E. Park, M. Lee, and S. Lim, "Switchable Bandpass/Bandstop Filter Using Liquid Metal Alloy as Fluidic Switch," *Sensors*, vol. 19, no. 5, p. 1081, Mar. 2019, doi: 10.3390/s19051081.

[17] W. F. Fang and A. P. Lee, "LCAT pump optimization for an integrated microfluidic droplet generator," *Microfluid Nanofluidics*, vol. 18, no. 5–6, pp. 1265–1275, May 2015, doi: 10.1007/s10404-014-1525-5.

[18] C. C. Glick *et al.*, "Rapid assembly of multilayer microfluidic structures via 3D-printed transfer molding and bonding," *Microsyst Nanoeng*, vol. 2, no. 1, pp. 1–9, Nov. 2016, doi: 10.1038/micronano.2016.63.

[19] D. Whitney, *Mechanical assemblies: their design, manufacture, and role in product development*. 2018. Accessed: Jun. 23, 2022. [Online]. Available: https://www.globalspec.com/reference/69914/203279/4-k-further-reading

[20] E. González, G. M.-I. M. and Wireless, and undefined 2019, “Integrated actuation of microfluidically reconfigurable mm-Wave SPST switches,” *ieeexplore.ieee.org*, Accessed: Jun. 23, 2022. [Online]. Available: https://ieeexplore.ieee.org/abstract/document/8768046/